Numerical modelling of desiccation cracking of clayey soil using a cohesive fracture method

Thi Dong Vo, Amade Pouya, Sahar Hemmati, Anh Minh A.M. Tang

Numerical modelling of desiccation cracking of clayey soil using a cohesive fracture method

Thi Dong Vo[1,2], Amade Pouya[2], Sahar Hemmati[1] and Anh Minh Tang[2]

[1] *Université Paris Est, IFSTTAR GERS/SRO, Marne-la-Vallée, France*

[2] *Université Paris Est, Laboratoire Navier (UMR8205), Marne-la-Vallée, France*

Corresponding author:

Anh Minh TANG

Ecole des Ponts ParisTech

6-8 avenue Blaise Pascal, Cité Descartes, Champs sur Marne

77455 Marne-la-Vallée, Cedex 2, France

Phone: +33 1 64 15 35 63

Email: anhminh.tang@enpc.fr

Abstract. This paper presents a numerical study on the desiccation cracking process of clayey soil. The initiation and propagation of cracks were investigated using finite element code, including the damage-elastic cohesive fracture law to describe the behaviour of cracks. The coupling between the hydraulic behaviour (moisture transfer in the soil matrix and in the cracks) and the mechanical behaviour (volume change of the soil matrix and development of cracks) were also considered. The results of a laboratory experiment performed on clay soil, taken from a literature review, were used to evaluate the numerical modelling. The results show that the code can reproduce the main trends observed in the experiment (*e.g.*, shrinkage related to drying, crack development). In addition, the numerical simulation enables the identification of other phenomena, such as the evolution of suction and stress related to drying and the development of a single crack. These phenomena are difficult to observe experimentally.

Key words: suction, evaporation, desiccation cracking, cohesive fracture, damage

1. Introduction

Desiccation cracking is a common phenomenon in soils and rocks. It involves a gradual moisture content reduction induced by evaporation from a geomaterial surface. This reduction in moisture content is accompanied by the invasion of air into the soil pores, increases in suction and the effective stress, and soil shrinkage. Shrinkage due to desiccation from the soil surface in restrained conditions (by frictional boundary conditions, concentration of stress or heterogeneity of soil) causes an increase in tensile stress, which induces the formation of crack networks when the stress reaches the tensile strength ([1]–[6]).

Due to the hydro-mechanical nature of the formation and propagation of desiccation cracking, this process influences various soil properties. On one hand, cracks change the permeability of soil from the hydraulic point of view. On the other hand, desiccation cracking changes the soil compressibility and decreases the mechanical strength, which could be one of the reasons for the instability of earth slopes ([7]–[9]).

The problem of desiccation cracking in soil has been studied using both experimental and theoretical approaches. Laboratory experimental studies ([5][10][11][12]) have mainly focused on the behaviour of clayey soil when drying specimens from a saturated state. The results demonstrate the effect of specimen dimensions, boundary conditions, soil properties, and drying conditions on the formation, propagation process and morphology of the crack network. Desiccation cracking has also been observed in situ ([13][14]), where the characteristic geometry of cracks, such as depth, thickness, density, spacing, and aperture, under the actual drying conditions were investigated. The results show that the onset of cracking depends on the mineralogy of the soil, the climatic conditions (temperature, relative humidity, rainfall), and the canopy. Following Li & Zhang ([13]), crack development can be described in three stages: initial, primary, and steady state. In the initial stage, few cracks develop with gradually decreasing water content. When the water content reaches a critical value for crack initiation,

cracks being to develop quickly, corresponding to the start of the primary stage. As the water content approaches the shrinkage limit of the soil, cracks develop slowly and reach a steady state.

Using numerical methods, the initiation and the propagation of cracks have been studied based on the theory of linear elastic fracture mechanics (LEFM), discrete element method (DEM), and finite elements method (FEM) with or without cohesive fracture and interface elements.

The propagation of cracks in solids has been studied using LEFM [15] to explain the magnitude of the depth and the spacing between desiccation cracks. This theory has been extended to unsaturated soil ([2][16][17]) to predict the optimal depth of cracks, which is a function of the suction profile and various soil properties (e.g., tensile strength, elastic modulus, Poisson's ratio, density). Konrad & Ayad [18] used LEFM to analyse the propagation of desiccation cracks of clays under evaporation. They used the principle of the effective stress distribution [3] to take into account the distribution of stress in soil and proposed the concept of virtual stress superposition to predict the average spacing between primary cracks. LEFM considers the propagation of only one individual crack and neglects the interaction between various cracks. In addition, LEFM assumes linear elastic soil behaviour; the nonlinearity that may be present in desiccation is thus ignored.

DEM, which considers the soil as an assemblage of discrete elements, has good potential for the simulation of desiccation cracking and was used in previous studies ([19]–[22]). Most active clay particles gather in elementary small structures called aggregates, which in turn gather in larger aggregates at various scales ([23][24]). In DEM, the clay soil is represented as an assemblage of aggregates linked by bonds, and the aggregates are simplified as spherical grains or other geometries [21]. The drying shrinkage kinetics of clay aggregates can be simulated by applying an explicit relationship between the size of the grains and the drying duration (or the water content). As the soil dries, the contact stiffness and tensile strength of the

aggregates increase with increasing suction. Crack initiation corresponds to the irreversible breakage of this bond when the magnitude of the traction (or shear) force exceeds the normal (or shear) contact bond strength. In addition, the non-linear behaviour of soil can be simulated by introducing the dependences of the soil properties on suction ([19][21][22]). Simulations have enabled the investigation of the effects of the soil sample dimensions, the interface between soil/mould, and soil shrinkage parameters on the development of desiccation cracks. More recently, Hirobe & Oguni [25] proposed a model that uses FEM to simulate hydraulic diffusion and PDS-FEM (particle discretisation scheme finite element method) to solve the mechanical problem of the formation of cracks. In this model, the elasticity and fracturing behaviour are modelled using the discretisation method, which uses a pair of conjugate geometries (Voronoi and Delaunay tessellations) to estimate the displacement and strain fields. A fracture propagates along the Voronoi cell boundaries as hydro-mechanical stress evolves and exceeds the prescribed material strength. This method was used to reproduce the morphology of the crack network and the evolution of the desiccation process. The principle of this work is similar to that of Asahina et al. [26]. Both demonstrated the influence of the specimen's thickness on the spacing of the formed cracks. Despite its efficiency to simulate desiccation cracks, DEM is considered more pertinent for the specimen scale than the structure scale.

Soil desiccation has been studied using FEM in previous research ([27]–[29]), but the development of cracks (which involves discontinuity in the medium) was not considered. For this reason, cohesive fracture and interface elements are usually introduced in FEM code to simulate the formation and propagation of cracks during desiccation. In the work of Sanchez et al. [30], joint elements were embedded like interface elements in the boundary of tetrahedral solid elements; the cracks propagated along the boundary of these solid elements. In this numerical analysis, the effect of evaporation was introduced as the volume shrinkage of solid

126 elements, and the simulation could be observed as purely mechanical. The prime interest of
127 this work was not to precisely reproduce the experimental observations but to determine the
128 ability of the proposed numerical technique to qualitatively capture the main trends and the
129 crack morphologies observed for different shapes, thicknesses and desiccation conditions.
130 Amarasiri & Kodikara [31] used cohesive cracks with a softening law that evolves during
131 desiccation when a crack is partially open. The model reproduced the number of cracks
132 developed with the moisture content evolution during a desiccation test but the desiccation
133 process with hydro-mechanical coupling was not considered.

134 In the present work, a hydro-mechanical model was developed to simulate the desiccation
135 cracking of clayey soil using a cohesive fracture method. The damage-elastic behaviour of
136 cohesive fracture [32] was used to model the initiation and propagation of cracks. The FEM
137 code POROFIS [33], for POROus FISsured media, was used to simulate the laboratory
138 desiccation tests reported by Sanchez et al. [11]. The results enabled the investigation of the
139 evolution of the stress, strain and hydric state (suction, degree of saturation) at different
140 locations in the soil specimen and the development of cracks during desiccation.

141 ## 2. Governing equations

142 This section briefly presents the governing equations of hydraulic and mechanical problems;
143 more details can be found in [32]–[34]. In the present model, soil is represented as a
144 homogenous porous medium containing a family of cohesive cracks. For the hydraulic
145 problem, the body can be subjected to pressure or flux boundary conditions. For the
146 mechanical problem, the body can be subjected to stress or displacement applied on its surface.
147 Other volumetric forces and gravity effects are not considered for this problem. The flow and
148 displacement fields in the body have to satisfy theses boundary conditions and the constitutive
149 equations detailed below.

2.1. Cohesive crack representation

In the finite elements method enriched by joint elements (JFEM) used here, the cohesive crack elements are represented by 4-node interface elements introduced by Goodman (1976) [35] for modelling rock joints. The joint elements are placed in the mesh on predetermined paths corresponding to potential crack propagation. For the mechanical problem, it is necessary to split the nodes on discontinuity lines and create joint elements to allow displacement discontinuities across fractures. However, in the hydraulic problem, at least for the fractures with infinite transverse conductivity considered here, and so with continuous pressure across the fracture, there is no need to split the nodes because the pressure has the same value on the two sides of the fracture. The specific mesh for this purpose is prepared using commercial tools (GID and DISROC) that are dedicated to meshing fractured media.

One of the limitations of the cohesive crack method is that the crack locations and pathways need to be predefined. However, this limitation can be addressed by using a multiple unbiased potential crack with a great density to minimise the spacing between cracks. This approach is chosen in the current work.

In this model, cohesive cracks are simulated as elements of zero thickness with a very small normal hydraulic conductivity and high stiffness at the beginning. For the mechanical behaviour of joint elements, the cohesive fracture law [32] is applied. A damage variable D is added to represent the process of damage through a decrease in the crack stiffness and the evolution of the yield surface. Under the effect of evaporation, the tensile stress increases with suction, corresponding to the increase in the normal stress of cohesive cracks. The initiation of cracks can be considered as the breakage of bonds through the degradation of the crack stiffness when the tensile stress reaches the tensile strength.

2.2. Hydraulic behaviour

The flow in the soil around cracks is governed by Darcy's law and satisfies the mass conservation condition. To establish hydraulic diffusion, the fluid mass m_f is calculated in unit volume:

$$m_f = \rho\phi S\,, \tag{1}$$

where ϕ is the porosity, ρ is the fluid density and S is the degree of saturation of the medium. For a saturated medium, $S = 1$, and the pore pressure p takes positive values.

The soil suction s is the difference between the gas (vapor and air) pressure p_g and the fluid pressure p in the pore space:

$$s = p_g - p \tag{2}$$

In the present work, gas pressure is zero. This means that in the unsaturated state, $s = -p$. By extending the pressure values to the negative domain, it is possible to represent, by a unique variable p, the pressure in the saturated state $p \geq 0$ and the suction in the unsaturated condition $p < 0$. Upon drying, the degree of saturation S is related to suction through the water retention curve, expressed by the function $S = f(p)$, based on the Van Genuchten model [36]:

$$\frac{S - S_{res}}{1 - S_{res}} = \frac{1}{(1 + (\alpha p)^n)^m}\,, \tag{3}$$

where S_{res} is residual degree of saturation and α, n and m are soil parameters.

The equation to determine the flow in the soil matrix with an assumption of incompressible fluid can be then written as follows [37,33]:

$$div(\frac{k}{\rho g}\nabla p) = C_M \frac{\partial p}{\partial t} + r\,, \tag{4}$$

with $C_M = S\left(\frac{1}{N} + \frac{\phi S^{'}}{S}\right)$, $r = S\frac{\partial \varepsilon_v}{\partial t}$, k is the soil hydraulic conductivity, g is acceleration due to gravity, N is the Biot modulus, $S^{'}$ is the derivative dS/dp calculated from the water retention curve, and ε_v is the volumetric deformation. The hydraulic conductivity k decreases during drying and is simulated as follows:

$$k = k_s\left(\frac{S - S_{res}}{1 - S_{res}}\right)^3, \tag{5}$$

where k_s represents the soil hydraulic conductivity in the saturated state.

For cracks, the transverse conductivity (between the two crack walls) is considered as infinite in the model, which implies that there is no pressure difference between two opposite walls of the crack, i.e., the pressure has the same value on both faces. It could also be represented by only one value of p at a given point along the crack line. The flow in the cracks is governed by the cubic law with the isotropic tangent conductivity of cracks (parallel to crack walls) denoted by c, which can be related to crack opening e and fluid viscosity μ through the following relation [38]:

$$c = \frac{e^3}{12\mu} \tag{6}$$

The equation to calculate the pressure for every location $\underline{s}$ along the crack surface can be then written as:

$$\nabla_s.(c\partial_s p) = r^{mf} + r^f, \tag{7}$$

where $r^{mf} = \|\underline{v}\|.\underline{n}$ and $r^f = \frac{\partial e}{\partial t}$.

In this equation, $\nabla_s.()$ designates the divergence in the crack. The velocity $\underline{v}$ must be related to the flow in the matrix and can be discontinuous, with values $\underline{v}^+$ and $\underline{v}^-$ for the two faces of

the crack. The term $\|\underline{v}\| = \left[\underline{v}^{+} - \underline{v}^{-}\right]$ represents the velocity discontinuity or the jump across the crack surface, which expresses the fluid mass exchange between the crack and the surrounding matrix, and $\underline{n}$ is the unit vector normal to the fracture surface. In Eq. (7), the source term r^{f} represents hydro-mechanical coupling and r^{mf} represents mass exchange between the matrix and the crack.

2.3. Mechanical behaviour

The mechanical behaviour of the soil matrix is formulated in terms of the effective stresses while the failure criterion of the cohesive cracks is based on the total stress. If the cracks are considered as very large pores, the suction in these pores is negligible, so it is reasonable to model their failure in terms of the total stress. This is in agreement with experimental observations ([19][22]), which show a small effect of the water content on the tensile strength of soils. This small effect is neglected in the present work. At the interface between the matrix element and the joint element, the continuity of the total stress is ensured.

The soil matrix is assumed to be an isotropic elastic linear material, and the relation between the effective stress and strain is expressed by the following equation:

$$\underline{\underline{\sigma}} = C : \underline{\underline{\varepsilon}} - Sp\underline{\underline{\delta}}, \tag{8}$$

where σ is the total stress, C is the elasticity tensor, ε is the strain tensor and $\underline{\underline{\delta}}$ is the identity matrix.

The elastic damage of the cohesive crack law is applied using the following equation:

$$\underline{\sigma} = (1 - D)\underline{\underline{R}}\,\underline{u} - b_f p\underline{n}, \tag{9}$$

where $\underline{\sigma}$ is the stress vector on the matrix/crack interface surface, $\underline{n}$ is the normal unit vector on this surface, $\underline{u}$ is the displacement discontinuity through this surface, $\underline{\underline{R}}$ is the crack stiffness tensor, b_f is Biot's coefficient of cracks and D is the damage variable. The

coefficient b_f is related to the ratio of the contact surfaces between the two walls of the crack to the total crack surface. A value of b_f =1 means the whole pressure in the crack is applied as mechanical action on the walls, which corresponds to the case of a totally damaged crack, without a bridge between the walls. When there is no damage (D = 0), $b_f = b_0$ should be very small. b_f increases with D and reaches 1 for D = 1. We express this relationship using the following law:

$$b_f = b_0 + (1 - b_0)D \tag{10}$$

The crack aperture (e) changes with the deformation from the initial value e_0 to:

$$e = e_0 + u_n, \tag{11}$$

where u_n is the normal component of u. The evolution of the damage variable D affects both the crack stiffness and the yield surface. The yield criterion is defined by a hyperbolic surface in the stress space, which corresponds to the following expression [32]:

$$F(\sigma, D) = \tau^2 - \sigma_n^2 \tan^2 \varphi + 2g(D)\sigma_c\sigma_n - g^2(D)\mathrm{C}^2, \tag{12}$$

with: $\sigma_c = \dfrac{C_{\mathrm{coh}}{}^2 + \sigma_R^2 \tan^2 \varphi}{2\sigma_R}$,

where τ; σ_n are the tangential and normal stresses of the joint, C_{coh} is the cohesion of the intact (undamaged) joint, φ is the friction angle, σ_R is the tensile strength of the intact joint and β is a coefficient representing the material's ductility.

The function $g(D)$ in Eq. (12) is defined such that the tensile strength, which is σ_R for the intact interface element, tends to zero for the totally damaged element: $g(D) = (1 - D)(1 - \beta \ln(1 - D))$

The damage evolution law in the cohesive fracture model [32] is given by the following relation:

260
$$\begin{cases} D = 0 & \text{for } u_n < u_0 \\ D = 1 - e^{-\frac{(u_n - u_0)}{\beta u_0}} & \text{for } u_n \geq u_0 \end{cases}, \quad (13)$$

261 where $u_0 = \frac{\sigma_R}{R_{nn}}$ is the elastic displacement limit, and R_{nn} is the normal component of the

262 joint stiffness.

263 ***2.4. Hydro-mechanical coupling***

264 The coupling between the mechanical and the hydraulic problems is performed through
265 sequential resolution of the two problems and the interactions between them. The schematic
266 view, shown in Fig. 1, represents the hydro-mechanical coupling for desiccation cracking
267 phenomena as resolved by POROFIS. For each time increment, the hydraulic problem is
268 calculated by solving Eq. (4) and Eq. (7). The outputs correspond to the soil suction, degree of
269 saturation and hydraulic conductivity of soil. These values are then used as inputs for the
270 mechanical problem. For the matrix, hydro-mechanical coupling (Eq. (8)) allows updating of
271 the effective stress in the soil matrix. Numerically, this coupling is performed by introducing
272 the term "free deformation", denoted by ε^L in Eq. (8), under the form: $\underline{\underline{\sigma}} = C : (\underline{\underline{\varepsilon}} - \underline{\underline{\varepsilon}}^L)$, in
273 which $\underline{\underline{\varepsilon}}^L = C^{-1}(Sp\underline{\underline{\delta}})$. For the elastic linear isotropic model, this free deformation can be
274 calculated as a function of the elasticity modulus E and the Poisson' ratio ν:
275 $\underline{\underline{\varepsilon}}^L = \frac{(1-2\nu)}{E} Sp\underline{\underline{\delta}}$. For cracks, the fluid pressure resulting from the resolution of the hydraulic
276 problem (Eq. (7)) is introduced in the mechanical problem (Eq. (9)) to calculate the crack
277 opening. Reciprocally, the matrix and the crack deformation resulting from the resolution of
278 the mechanical problem are then introduced into the hydraulic problem through source term
279 r, which is related to the volumetric strain of the matrix (Eq. (4)), and r^f, representing the
280 crack opening evolution (Eq. (7)). In addition, the crack opening e is used to update the
281 hydraulic conductivity of the crack (Eq. (6)). This coupling implies that as soon as the crack is

mechanically opened, its hydraulic conductivity increases quickly and potentially conducts more fluid through it.

3. Numerical simulation

The hydro-mechanical finite element code presented above was used to simulate the desiccation experiments reported by Sanchez et al. [11]. In this test, a 100 mm diameter and 13 mm thick circular plate of organic silt (30% sand, 57% silt and 13% clay) was prepared in a slurry state and then air-dried. By using a 2D profile laser technique, various soil characteristics (e.g., volume change, water loss, and crack development) were observed during drying.

To simulate the experiments, various data related to the tested materials were collected to determine the parameters used in the numerical model. Fig. 2 shows the water retention curve obtained for the same soil but from a compacted specimen [39]. The degree of saturation at low suction (0.001 MPa) is still significantly lower than 1 because of hysteresis. Therefore, the water retention curve used in the present work starts in the saturated state (S = 1) for the lowest suction. Various works have found that desiccation cracks initiate at soil suction close to the air-entry value ([5][12]). The experimental data indicated an air-entry value of approximately 100 kPa, so the model was fitted to the experimental data around this value. The parameters selected for the water retention curve (Eq. 3) were then: $\alpha = 9.81\ MPa^{-1}$, $n = 1.60$, and $m = 1 - 1/n = 0.375$

The soil compressibility was estimated following the oedometer compression curve obtained on the same soil but in a compacted state [40]. The volumetric strain for these data is plotted versus the vertical stress for the studied soil (Fig. 3). In the present work, the soil compressibility parameters were chosen ($E = 1$ MPa and $\nu = 0.3$) to fit the experimental data in

the low stress range (up to 0.3 MPa), which should be the range of suction corresponding to the crack development.

The hydraulic conductivity in the saturated state, $k_s = 10^{-8} m/s$, was selected following the method proposed by Mesri et al. [41], which estimates the hydraulic conductivity of fine-grained soils from the void ratio, clay fraction and soil activity.

As explained above, the cohesive crack law was used to model the formation and propagation of desiccation cracks. The cohesive crack parameters influence the behaviour of the model, and its determination plays an important role. Several studies indicated that desiccation cracking occurs mainly in mode I ([15][16][18]). Amarasiri & Kodikara [42] presented results of fracture tests performed on beams of compacted clay at various moisture contents. A bi-linear cohesive crack law was used to model the development of bridging stress across an opening crack, which progressively decreased from the tensile strength to zero as the two faces separated. The properties of the cohesive crack (e.g., fracture energy, tensile strength, and crack opening at which the normal cohesive stress drops to zero) were determined by back-analysis. In the present work, the main parameters of a cohesive crack are: normal component of the joint's stiffness tensor $\underline{\underline{R}}$ (R_{nn}), tensile strength σ_R, and initial crack thickness e_0. The tensile strength σ_R was chosen close to the air-entry value at which the crack initiated, as suggested by Peron et al.[5], Tang et al. [12], and Shin & Santamarina [43]. The initial values of the normal stiffness R_{nn} were set sufficiently high and that of the hydraulic conductivity (related to the initial thickness e_0) was set sufficiently small to have negligible effects on the global elasticity and permeability of the model before cracking. The parameter β corresponds to the ductility of material and can be fitted from the experimental curves [44]. In this work, it was set equal to 1, which indicates that the tensile stress of the fracture starts to decrease at the onset of damage. The parameters C_{coh} and φ do not affect

329 mode I crack propagation, which is the case of the present work. However, these parameters
330 must satisfy the inequality $C_{\text{coh}} / \tan\varphi > \sigma_R$ for the hyperbolic surface. Therefore, C_{coh} was set
331 to $C_{\text{coh}} = 1.5\sigma_R \tan\varphi$. Table 1 summarises the main parameters of soil and cohesive cracks
332 used in the simulation.

333 To simulate the test performed, a 2D mesh in the plane strain conditions shown in Fig. 4 was
334 used. Its width was equal to the diameter of the sample (100 mm), and its height was equal to
335 the initial height of the sample (13 mm). The experimental observation showed were 4 cracks
336 (for a typical cross section) after 24 hours of drying, and these cracks propagated vertically in
337 depth. As mentioned above, in POROFIS, a large unbiased number of cracks and pathways can
338 be introduced. Crack development is dictated by the behaviour of the model. However, in the
339 present work, to optimise the calculation cost by always ensuring adequate mesh density, 100
340 vertically oriented cohesive cracks were distributed regularly with a spacing of *d = 1 mm* in the
341 mesh (see Fig. 4).

342 For the mechanical boundary conditions, the displacements at the bottom, the right and left
343 sides were fixed, while the top of the mesh (representing the soil surface) was free to move.
344 For the hydraulic boundary conditions, no flux was allowed at the bottom, right and left sides
345 of the mesh. On the top of the mesh, homogenous flux, calculated based on the evaporation
346 rate estimated from the test, was imposed. The details of the determination of this flux are
347 given below.

348 The experimental observation of soil water evaporation ([45]–[48]) from the saturated state
349 generally indicated three main phases. The first phase corresponds to a constant evaporation
350 rate with elapsed time. In this phase, suction develops slowly, and the soil remains in a
351 saturated state. In the second phase, the evaporation rate decreases rapidly and soil suction
352 increases significantly. In the last phase, the evaporation rate reaches the residual value, which

353 depends on the soil characteristics. In the present work, the evaporation rate was imposed on
354 the top of the mesh as a function of the suction calculated at the soil surface (see Fig. 5). To
355 obtain the experimental data plotted in this figure, the relationship between the evaporation rate
356 and the average degree of saturation of the soil specimen in the experiment was calculated
357 from the experiment (Fig. 5*a*). Then, by combining this information with the water retention
358 curve (Fig. 2), the relationship between the evaporation rate and soil suction was determined
359 (Fig. 5*b*). The actual evaporation rate (E_a) was calculated based on the soil suction at the
360 surface, as expressed below:

361
$$\begin{cases} E_a = E_p & \text{if } |s| \le |s_0| \\ E_a = E_p \exp\left[-\alpha(s - s_0)\right] & \text{if } |s| > |s_0| \end{cases}, \tag{14}$$

362

363 where E_p is the potential evaporation rate, which represents the evaporation capacity of soil
364 under completely saturated conditions, s is the actual suction at the surface, s_0 is a suction of
365 the onset of the second phase in the evaporation process, and α is a curve coefficient. Wilson
366 et al. [46] measured the actual evaporation rate using a drying column test. The evaporation
367 rate evolution showed that the first phase had a constant evaporation rate of 8 mm/day. During
368 the second phase, a slight decrease in the evaporation rate began when the sand surface became
369 visually dry. This corresponds to a water content at the sand surface of slightly less than 2%;
370 thus, the suction corresponding to this water content on the water retention curve was
371 approximately 0.5-0.6 MPa. Moreover, Wilson et al. [49] found that the actual rate of
372 evaporation began to decline when the value of the total suction exceeded approximately 3
373 MPa. This conclusion was obtained from three tested soils: clay, silt, and sand.

374 In the present work, the parameters selected by assuming the exponential form of evaporation
375 evolution (Eq. (14)) and by fitting the experimental curve were: $E_p = 0.3$ *mm/h,* $\alpha = 1.857$ and
376 $s_0 = 0.3$ *MPa*. Note that s_0 = 0.3 MPa corresponds to an average degree of saturation S = 0.5

(following the water retention curve, see Fig. 2), which corresponds to the beginning of the decrease in the evaporation rate during drying (see Fig. 5a).

4. Results

Fig. 6a presents the morphology of the specimen during drying. This figure is plotted from the numerical results in Fig. 6b, where the distribution of horizontal displacement was equally added. The proposed model reproduced the main phases observed in the experimental test. At the beginning of the test, only settlement at the soil surface was observed without cracking (*i.e.*, with t = 3 h). The two first cracks appeared close to the two lateral walls at t = 4 h. During the next 4 h, the aperture (opening) of the cracks increased and no more cracks appeared. After t = 8 h, the crack network developed very quickly and, the cracks appeared with the same spacing of approximately 6-10 mm (t = 9 and 10 h). At t = 12 h, the specimen had 17 cracks and 100 cohesive joints were placed in the model. The evolution of suction measured at the top and at the bottom of the specimen (point A and point B in Fig. 4) is shown in Fig. 7*a*. The suction at these two points was similar, indicating that the suction was homogenous in the specimen during the drying test. In addition, when the first crack appeared (at t = 4 h), the soil suction was approximately 0.08 MPa, smaller than the air-entry value of 0.1 MPa. The suction corresponding to the rapid development of several cracks (at t = 8 – 9 h) was approximately 0.2 MPa. After 12 h of drying, the soil suction reached approximately 0.3 MPa. The degree of saturation calculated at these two points is also plotted in Fig. 7*b*. These values were slightly lower than the average degree of saturation measured from the experiment. However, the trend observed in the numerical simulation was similar to that observed from the experiment: a progressive decrease in the degree of saturation during drying with the degree of saturation remaining high after 12 h of drying.

In the experimental work, the measured 2D profiles were used to calculate the three components of soil shrinkage for a generic cross section: vertical displacement of the top surface (settlement), lateral shrinkage (gap), and cracks (see Fig. 8). This process made it possible to determine the three components of the deformation mentioned above from the simulation. The results of the simulation are shown in Fig. 9. At the beginning (t = 0 – 3 h), the shrinkage corresponds only to settlement. For t = 3-8 h, a gap appears, but its area remains small, and the total shrinkage area is still related to settlement. From t = 8 h, cracks appear quickly, and there is an abrupt increase in crack area. The increase in crack area is the main cause of shrinkage area in this phase. In the experiment, drying was performed for 24 h, while in the present work, the simulation was stopped after 12 h. Additionally, the mechanical behaviour of the soil matrix is linearly elastic in this work. This assumption is reasonable only when the soil strain remains small.

In addition to the evolution of the soil parameters, which can be experimentally observed, the numerical simulation enables in depth analysis of the processes related to crack opening. Two families of cracks can be identified: (*i*) the two first cracks appear close to the boundary of the soil specimen in contact with the rigid mould, which is defined as the lateral gap in the experimental work; and (*ii*) the cracks develop in the middle of soil sample, which is defined as "cracks" in the experimental work. The mechanisms related to the opening of these two families are shown separately in Figs. 10-13.

Fig. 10 presents the isochrones of the normal stress, damage variable and opening of all joint elements along the line of the gap on the left side (X = 1 mm). At the beginning (t < 3.505 h), the tensile stresses of these joint elements increase gradually during drying, but they remain smaller than the tensile strength $\sigma_R = 0.09$ MPa; thus, no damage occurs. At t = 3.505 h, the tensile stress of some joint elements on the top surface approaches the soil tensile strength (Fig.

10*a*). The elastic limit is reached and the damage phase begins. At this moment, the crack remains closed at the top, no opening of the crack is observed (see Fig. 10*c*) and the sample shows only settlement without cracking. For the next step (t = 3.510 h), some joint elements on the top surface (Y > 12 mm) are completely damaged, *i.e.*, their damage variable reaches its maximum value (equal to 1) (Fig. 10*b*). This total damage relaxes the normal stress of these joint elements (Fig. 10*a*). The bridge between the two surfaces of the crack is considered to be completely broken, and the crack is opened from the surface to its extremity. Fig. 10*a* shows that there is a stress singularity in the crack tip, which is in agreement with the LEFM [50]. For the following joint elements, normal stress continues to develop, the damage phase starts for some joint elements while others remain in the elastic phase, with damage variable equal to 0. This process is repeated in all joint elements along the crack line, and the crack opens gradually in depth (from t = 3.510 h to t = 3.530 h). The crack then propagates from the top to the bottom of the specimen in a short period (approximately 0.03 h). After this propagation in depth, all joint elements in the crack line are completely damaged, their normal stress decreases to zero, and the damage variable remains 1.

The opening of this crack (X = 1 mm) during the next step of drying (for t = 4 – 12 h) is presented in Fig. 11. The crack aperture continues to increase from t = 4 h to t = 8 h. After t = 8 h, other cracks appear, and the aperture of the crack decreases suddenly from t = 1.7 mm to 0.3 mm and remains at this value after 3 hours of drying.

Fig. 12 shows the isochrones of the normal stress, damage variable and opening of all joint elements along the line of the crack at X = 35 mm (see Fig. 6). At the beginning of drying, from t = 1 h to t = 8.50 h, the tensile stress of these joint elements increases gradually while drying. At t = 8.50 h, the tensile stress of the elements close to the bottom (at Y = 0.6-1 mm) approaches the soil tensile strength $\sigma_R = 0.09$ MPa but that of the other joint elements (with Y

448 >1 mm) remains smaller than the tensile strength. This is the elastic phase of these joint
449 elements, and no damage occurs. At t = 8.95 h, some joint elements near the bottom of the
450 specimen (Y < 4 mm) are completely damaged, *i.e.*, their damage variable reaches its
451 maximum (equal to 1) (Fig. 12*b*). The normal stresses of these joint elements are relaxed to
452 zero (Fig. 12*a*). The total damage indicates that all the bridge or contact points between the two
453 surfaces of the crack are completely broken, and the crack is opened from the first damaged
454 element (very close to the bottom of the specimen) to its extremity (Fig. 12*c*). The process of
455 damage is continued along the crack line, and the crack is opened gradually upward (from t =
456 8.50 h to t = 9.10 h). This crack propagates along the crack line and is detected from the top
457 surface at t = 9.10 h. After this propagation along the thickness of the sample, all joint elements
458 in the crack are completely damaged, their normal stress is relaxed to zero and the damage
459 variable remains 1. Fig. 12*c* shows the evolution of the crack opening during the propagation.
460 The crack is initiated from the element near the bottom of the sample, and there is no suction
461 gradient in the sample (Fig. 7*a*). However, when the crack is detected from the surface, the
462 crack aperture at the top is always larger than the one at the bottom. The top surface is free to
463 move, while the bottom displacement is restrained by the prescribed boundary conditions. The
464 opening of this crack during the next step of drying (for t = 10–12 h) is presented in Fig. 13.
465 After propagation to full depth, the crack aperture continues to increase until t = 10 h. Then,
466 other cracks appear near this crack (Fig. 6), and the aperture of the crack decreases suddenly
467 from t = 1.6 mm to 0.3 mm.

468 Fig. 14 shows the normal stress of all cohesive cracks on the top surface for X = 0-50 mm. At t
469 = 3.5 h, the tensile stress is 0.04 MPa for X > 20 mm, but it reaches 0.09 MPa at X = 1 mm. At
470 t = 4 h, a gap appears at X = 1 mm (represented by a mark in the figure); the tensile stress of
471 this gap is relaxed and drops to zero. The appearance of this gap induces a reduction in the
472 tensile stress of nearby cohesive cracks. The effect of this interaction decreases with distance.

From t = 4 h to t = 8 h, no more cracks appear; thus, the tensile stress continues to increase. At t = 8.3 h, a crack at X = 6 mm appears, decreasing the tensile stress. This phenomenon is repeated at t = 8.5 h and t = 8.6 h, when cracks appear at X = 11 mm and X = 16 mm, respectively. Interaction between cracks occurs when a new crack appears, creating a stress relief zone in the surface in which the stresses are reduced [18], while the prescribed boundary condition at the bottom of the specimen concentrates the tensile stress in this location.

Fig. 15 shows the evolution of the tensile stress of the cohesive crack at X = 35 mm for a joint element on the top surface (Y = 13 mm) and close to the bottom of the specimen (Y = 0.61 mm). The tensile stress of the joint element near the bottom of the specimen is higher than that of the specimen on the surface. At t = 8.5 h, the tensile stress of the joint element near the bottom approaches the tensile strength (0.09 MPa) while the tensile strength of the joint element on the top surface reaches 0.06 MPa. Due to the damage cohesive crack in the model, when the tensile stress reaches the soil tensile strength, the damage process occurs and the crack initiates, as explained above.

5. Discussions

In the present work, FEM code, including hydro-mechanical coupling and cohesive crack elements, was used to simulate the desiccation cracking of soils. The matrix behaviour was assumed to be isotropic linear elastic. Elastic behaviour was also used in previous research to model desiccation cracking ([25][28]). In the present work, the elastic modulus was fitted to the experimental data in the range of low stress (smaller than 0.3 MPa, see Fig. 3). After 12 h of desiccation, the suction (and soil stress) remained in this range (see Fig. 7*a*).

Literature review ([3][15][16][18]) showed that desiccation cracking occurs essentially via mode I, indicating that cracking in soils results from the development of tensile stress. As soil undergoes drying, it exhibits a suction change, which causes the inter-particle force to increase.

497 An apparent cohesion term is thus created, and consequently, a tensile strength term. Kim &
498 Hwang [51] attempted to directly relate tensile strength to the normal inter-particle force
499 calculated from micro-scale considerations. Other researchers proposed direct relations
500 between the decrease in water content and the tensile strength through experimental analysis
501 ([22][51]). Peron et al. ([5][49]) performed desiccation tests on three soils and found that
502 cracking initiates at the end of the first stage of drying. In the present work, the simulation
503 results showed that the first cracks initiate at approximately 4.0 h, when suction equals 0.08
504 MPa. At that moment, the evaporation rate is at its maximum value (E_p), see Fig. 5.

505 A 2D mesh was used for the model in the present work (Fig. 4), while the experiment was
506 performed with a cylindrical specimen. The prime interest of this work is not a quantitative
507 prediction of the experimental results but a qualitative reproduction of the main trends and
508 crack development during drying. Various experimental studies ([25][30][49][52]) show that
509 the crack network would be different for two cases: (*i*) for the case of a long bar (similar to the
510 model in the present work), the cracks are formed successively and perpendicular to the long
511 side of the specimen; (*ii*) for the case of a circular sample or a rectangular slab, the cracks can
512 appear simultaneously or successively to create a crack network. In the experiment considered
513 in the present work, the evolution of a typical section was analysed. A 3D mesh would then be
514 necessary to accurately reproduce the crack pattern in this case. In the present work, only a 2D
515 mesh was used. Most of numerical studies use 2D mesh ([19][20][22][25][31]), while few
516 works consider a 3D mesh ([21][30]). Although the 3D crack pattern was not simulated in the
517 present work, the result obtained in the 2D study improves the understanding of shrinkage
518 cracking mechanisms.

519 The model was able to reproduce correctly the main phases of the desiccation and the
520 development of soil shrinkage versus elapsed time (Fig. 6,7, and 9). Initially, shrinkage is

associated with settlement only. In the model, settlement without cracking corresponds to the elastic phase of cohesive cracks, in which the tensile stress increases with drying but remains smaller than the tensile strength. The damage phase begins when the tensile stress of cohesive cracks reaches the soil tensile strength and crack initiation is observed. In the present work, the crack network appears quickly at t = 8.3 h. This time can be observed as the critical time in the cracking development process. Li et al. [13] studied desiccation crack initiation and development of the ground surface and showed that desiccation cracks develop in three stages: initial, primary and steady states. In the first stage, few cracks develop with gradually decreasing water content, and a critical suction value exists for crack initiation after which cracks appear and propagate quickly.

Kodikara & Costa [6] presented two controlling factors in desiccation cracking. The first is the tensile stress distribution when the material is restrained against shrinkage. The tensile stress distribution depends on the boundary conditions and the material stiffness and dictates where the cracks initiate. The second factor is related to the flaws and/or pores within the material, where cracks can initiate at a stress level lower than the maximum stress developed within the material. Costa & Kodikara [55] observed that cracks could initiate even at suction of approximately 1 kPa for a clay slurry because of the large pores. In this work, cohesive cracks were placed equidistantly with the same parameters. In addition, there was no suction gradient in the sample (Fig. 7*a*). The heterogeneity of the material properties and the flaw factors are therefore neglected in this work. As a result, crack initiation depends only on the tensile stress distribution, which is mainly controlled by the boundary conditions.

The results obtained from the present work show that the discontinuity initially develops at the gaps (Fig. 6). This phenomenon can be explained by the normal stress distribution on the top surface at t = 3.5 h (see Fig. 14), where the normal stress is highest at X = 1 mm. In addition, the development of the crack network in Fig. 6 shows that the cracks progressed from the two

546 “gaps” beside the lateral boards to the middle of the sample, in agreement with the
547 observations in [11] but not a general trend [19]. In the present work, this can be explained by
548 the fact that when the gaps are created near the lateral boundaries, the stress field in the sample
549 is no longer uniform and induces new cracks that preferentially progress from the lateral
550 boundaries towards the centre of the sample. In addition, Fig. 6 shows that the crack opening
551 depends on its location. The two lateral boards are fixed, so when two faces of a crack
552 separate, the face closer to the boundary side presents a smaller displacement than the other
553 side. These cracks thus present a V shape that is not symmetric and depends on their location,
554 but the global configuration of the crack shape and location is symmetric with respect to the
555 axis of the sample.

556 The present work showed that in some conditions cracks could develop from near the bottom
557 of the specimen and propagate to reach the top surface. This can be explained in the model by
558 the combined effects of boundary conditions at the bottom that cause stress concentration at
559 these locations and the stress reduction on the top surface due to the onset of adjacent cracks
560 (Fig. 14 and 15). In this numerical model, all the joint elements are fixed to the bottom.
561 Therefore, the crack aperture cannot be observed from the bottom, similar to the observations
562 in a previous experiment ([11]). Weinberger [56] studied the initiation and growth of cracks
563 during desiccation of stratified muddy sediment and found that in the absence of surface
564 defects, crack origins are consistently located at or near the bottom of the polygons. During
565 drying, cracks initiated at the bottom and propagated vertically upward and laterally towards
566 adjacent cracks. The crack propagation from the bottom to the full depth was also observed by
567 Costa et al. [57] while testing desiccation cracking on three potato starch specimens.

568 # 6. Conclusions

569 In this study, a desiccation cracking experiment was simulated using a hydro-mechanical
570 model where (*i*) hydraulic diffusion under evaporation, (*ii*) the shrinkage of a soil sample and
571 (*iii*) the initiation and propagation of desiccation cracks, among others couplings, were
572 considered. The diffusion equation included the evolution of the soil and crack hydraulic
573 properties (degree of saturation, soil hydraulic conductivity and crack hydraulic conductivity,
574 the mass exchange between soil matrix/cracks), and the deformation processes of the soil and
575 the crack were equally taken into account. Finite element method code, including cohesive
576 fractures model, was used to simulate the development of cracks. The coupling between the
577 hydraulic and mechanical phenomena was performed through an iterative process passing
578 from the hydraulic problem resolution to the mechanical problem resolution and vice versa.

579 Cohesive cracks were embedded into the model to simulate potential cracks. By including a
580 large number of joint elements in the mesh, the model enables the detection of crack
581 development during drying. The results of the numerical simulation show good agreement with
582 the experimental data in terms of hydraulic diffusion, crack initiation, shrinkage evolution and
583 the chronology of desiccation phases (settlement without cracking and the formation and
584 propagation of cracks). The present work highlighted the importance of boundary conditions
585 when studying desiccation cracking. The simulation of a desiccation test revealed that cracks
586 could develop, in some cases from near the bottom of the specimen, and propagate towards the
587 top surface, even if the water evaporation occurs only from the top. The results of the present
588 work indicate that the proposed hydro-mechanical coupled model using the cohesive fracture
589 law for modelling crack propagation can accurately reproduce the hydro-mechanical coupled
590 phenomena related to shrinkage and crack formation during drying of clayey soil.

591 ## Acknowledgement

The Authors would like to thank Prof. Farimah Masrouri and Dr. Jean-Bernard Karzmierczak for their valuables comments.

References

[1] E. M. Kindle, "Some Factors Affecting the Development of Mud-Cracks," *J. Geol.*, vol. 25, no. 2, pp. 135–144, 1917.

[2] J. T. K. Lau, "Desiccation cracking of soils," 1987.

[3] A. N. Abu-Hejleh and D. Znidarcic, "Desiccation Theory for Soft Cohesive Soils," *J. Geotech. Eng.*, vol. 121, no. June, pp. 493–502, 1995.

[4] Towner, "The Mechanics of Cracking of Drying," *J. agric. Engng Res*, vol. 36, pp. 115–124, 1987.

[5] H. Peron, T. Hueckel, L. Laloui, and L. B. Hu, "Fundamentals of desiccation cracking of fine- grained soils : experimental characterisation and mechanisms identification," *Can. Geotech. J.*, vol. 46, pp. 1177–1201, 2009.

[6] J. Kodikara and S. Costa, "Desiccation Cracking in Clayey Soils: Mechanisms and Modelling," *Multiphysical Test. Soils Shales*, pp. 21–32, 2013.

[7] R. Baker, "Tensile strength, tension cracks, and stability of slopes," *Soils Found.*, vol. 21, no. 2, pp. 1–17, 1981.

[8] N. Yesiller, C. J. Miller, G. Inci, and K. Yaldo, "Desiccation and cracking behavior of three compacted landfill liner soils," *Eng. Geol.*, vol. 57, pp. 105–121, 2000.

[9] G.H.Omidi, J.C.Thomas, and K.W.Brown, "Effect of desiccation cracking on the hydraulic conductivity of a compacted clay liner," *Water. Air. Soil Pollut.*, vol. 89, pp. 91–103, 1996.

[10] J. K. Kodikara, S. L. Barbour, and D. G. Fredlund, "Desiccation cracking of soil layers," in *UNSAT ASIA 2000*, 2000, pp. 693–698.

[11] M. Sanchez, A. Atique, S. Kim, E. Romero, and M. Zielinski, "Exploring desiccation cracks in soils using a 2D profile laser device," *Acta Geotech.*, vol. 8, no. 6, pp. 583–596, Oct. 2013.

[12] C.-S. Tang, B. Shi, C. Liu, W.-B. Suo, and L. Gao, "Experimental characterization of shrinkage and desiccation cracking in thin clay layer," *Appl. Clay Sci.*, vol. 52, pp. 69–77, Apr. 2011.

[13] J. H. . Li and L. M. Zhang, "Study of desiccation crack initiation and development at ground surface," *Eng. Geol.*, vol. 123, pp. 347–358, 2011.

[14] J.-M. Konrad and R. Ayad, “Desiccation of a sensitive clay: field experimental observations,” *Can. Geotech. J.*, vol. 34, pp. 929–942, 1997.

[15] A. H. Lachenbruch, “Depth and spacing of tension cracks,” *J. Geophys. Res.*, vol. 66, no. 12, p. 4273, 1961.

[16] P. H.Morris, J.Graham, and D. J.Williams, “Cracking in drying soil,” *Can.Geotech*, vol. 29, pp. 263–277, 1991.

[17] D. . Fredlund and N. R. Morgenstern, “Constitutive relations for volume change in unsaturated soils,” *Can. Geotech. J.*, vol. 13, pp. 261–276, 1976.

[18] J.-M. Konrad and R. Ayad, “An idealized framework for the analysis of cohesive soils undergoing desiccation,” *Can. Geotech. J.*, vol. 34, pp. 477–488, 1997.

[19] A. L. Amarasiri, J. K.Kodikara, and S. Costa, “Numerical modelling of desiccation cracking,” *Int. J. Numer. Anal. Methods Geomech.*, vol. 35, pp. 82–96, 2010.

[20] H. Peron, J. Y. Delenne, L. Laloui, and M. S. El Youssoufi, “Discrete element modelling of drying shrinkage and cracking of soils,” *Comput. Geotech.*, vol. 36, no. 1–2, pp. 61–69, Jan. 2009.

[21] J. Sima, M. Jiang, and C. Zhou, “Numerical simulation of desiccation cracking in a thin clay layer using 3D discrete element modeling,” *Comput. Geotech.*, vol. 56, pp. 168–180, Mar. 2014.

[22] R. A. Stirling, “Multiphase Modelling of Desiccation Cracking in Compacted Soil,” Newcastle University, 2014.

[23] V. Ferber, J.-C. Auriol, Y.-J. Cui, and J.-P. Magnan, “Wetting-induced volume changes in compacted silty clays and high-plasticity clays,” *Can. Geotech. J.*, vol. 45, no. 2, pp. 252–265, Feb. 2008.

[24] E. E. Alonso, J. Vaunat, and A. Gens, “Modelling the mechanical behaviour of expansive clays,” *Eng. Geol.*, vol. 54, no. 1–2, pp. 173–183, Sep. 1999.

[25] S. Hirobe and K. Oguni, “Coupling analysis of pattern formation in desiccation cracks,” *Comput. Methods Appl. Mech. Eng.*, May 2016.

[26] D. Asahina, J. E. Houseworth, J. T. Birkholzer, J. Rutqvist, and J. E. Bolander, “Hydro-mechanical model for wetting/drying and fracture development in geomaterials,” *Comput. Geosci.*, vol. 65, pp. 13–23, Apr. 2014.

[27] R. Rodriguez, M. Sanchez, A. Ledesma, and A. Lloret, “Experimental and numerical analysis of desiccation of a mining waste,” *Can. Geotech. J.*, vol. 658, pp. 644–658, 2007.

[28] H. Péron, L. . Hu, L. Laloui, and T. Hueckel, “Numerical and Experimental Investigation of Desiccation of Soil,” no. 3, pp. 3–8, 2007.

[29] O. P. Coussy and S. Brisard, “Prediction of drying shrinkage beyond the pore isodeformation assumption,” *J. Mech. Mater. Struct.*, vol. 4, no. February, pp. 263–279, 2009.

[30] M. Sánchez, O. L. Manzoli, and L. J. N. Guimarães, “Modeling 3-D desiccation soil crack networks using a mesh fragmentation technique,” *Comput. Geotech.*, vol. 62, pp. 27–39, Oct. 2014.

[31] A. L. Amarasiri and J. K. Kodikara, “Numerical Modeling of Desiccation Cracking Using the Cohesive Crack Method,” *Int. J. Geomech.*, vol. 13, pp. 213–221, 2013.

[32] A. Pouya and P. Bemani, “A damage-plasticity model for cohesive fractures,” *Int. J. Rock Mech. Min. Sci.*, vol. 73, pp. 194–202, 2015.

[33] A. Pouya, “A finite element method for medeling coupled flow and deformation in porous fractured media,” *Int. J. Numer. Anal. Methods Geomech.*, vol. 32, 2015.

[34] A. Pouya, T. D. Vo, S. Hemmati, and V. L. Nguyen, “Modélisation numérique de la fissuration hydrique d’un sol non saturé,” in *SEC2015*, 2015, pp. 1–10.

[35] R. E. Goodman, *Methods of Geological Engineering in Discontinuous Rocks*. 1976, p. 484.

[36] M. T. van Genuchten, “A Closed-form Equation for Predicting the Hydraulic Conductivity of Unsaturated Soils1,” *Soil Sci. Soc. Am. J.*, vol. 44, p. 8, 1980.

[37] L. a. Richards, “Capillary Conduction of Liquids Through Porous Mediums,” *Physics (College. Park. Md).*, vol. 1, no. 5, p. 318, 1931.

[38] R. W. Zimmerman and G. S. Bodvarsson, “Hydraulic Conductivity of Rock Fractures,” 1994.

[39] G. El Mountassir, M. Sánchez, E. Romero, and R. a a Soemitro, “Behaviour of compacted silt used to construct flood embankment,” *Proc. ICE - Geotech. Eng.*, vol. 164, no. 3, pp. 195–210, Jun. 2011.

[40] G. El Mountassir, M. Sánchez, and E. Romero, “An experimental study on the compaction and collapsible behaviour of a flood defence embankment fill,” *Eng. Geol.*, vol. 179, pp. 132–145, Sep. 2014.

[41] G.Mesri and Y.K.Choi, “Settlement of Embankments on Soft Clays,” *J. Geotech. Geoenvironmental Eng.*, vol. 111, no. 4, pp. 441–464, 1985.

[42] A. L. Amarasiri, S. Costa, and J. K. Kodikara, “Determination of cohesive properties for mode I fracture from compacted clay beams,” *Can. Geotech. J.*, vol. 38, pp. 1163–1173, 2011.

[43] H. Shin and J. C. Santamarina, “Desiccation cracks in saturated fine-grained soils : particle-level phenomena and effective-stress analysis,” *Géotechnique*, vol. 61, no. 11, pp. 961–972, 2011.

[44] T. Backers, “Fracture Toughness Determination and Micromechanics of Rock Under Mode I and Mode II Loading,” 2004.

[45] G. W. Wilson, “Soil Evaporative Fluxes for Geotechnical Engineering Problems,” 1990.

[46] G. W. Wilson, D. G. Fredlund, and S. L. Barbour, “Coupled soil-atmosphere modelling for soil evaporation,” *Can. Geotech. J.*, vol. 31, no. 2, pp. 151–161, Apr. 1994.

[47] W. Song, Y. Cui, A. M. Tang, W. Ding, and T. D. Tran, “Experimental study on water evaporation from sand using environmental chamber,” *Can.Geotech*, vol. 51, pp. 115–128, 2014.

[48] W.-K. Song, Y.-J. Cui, A. M. Tang, W.-Q. Ding, and Q. Wang, “Experimental study on water evaporation from compacted clay using environmental chamber,” *Can.Geotech*, pp. 1–12, 2016.

[49] G. W. Wilson, D. G. Fredlund, and S. L. Barbour, “The effect of soil suction on evaporative fluxes from soil surfaces,” *Can.Geotech*, no. 1990, 1997.

[50] H. M. Westergaard, “Bearing pressure and cracks,” *J. Appl. Mech.*, pp. 49–53, 1939.

[51] T.-H. Kim and C. Hwang, “Modeling of tensile strength on moist granular earth material at low water content,” *Eng. Geol.*, vol. 69, no. 3–4, pp. 233–244, Jun. 2003.

[52] G. D. Towner, “The Tensile Stress Generated in Clay through Drying,” *J. agric. Engng Res*, vol. 37, pp. 279–289, 1987.

[53] H. Peron, L. Laloui, T. Hueckel, and L. B. Hu, “Desiccation cracking of soils,” *Fail. Multiph. geomaterials*, vol. 13, pp. 869–888, Aug. 2009.

[54] H. Nahlawi and J. K. Kodikara, “Laboratory experiments on desiccation cracking of thin soil layers,” *Geotech. Geol. Eng.*, vol. 24, no. 6, pp. 1641–1664, Dec. 2006.

[55] S. Costa and J. Kodikara, “Evaluation of J Integral for Clay Soils Using a New Ring Test,” *Geotech. Test. Journalournal*, vol. 35, no. 6, pp. 981–989, 2012.

[56] R. Weinberger, “Initiation and growth of cracks during desiccation of stratified muddy sediments,” *J. Struct. Geol.*, vol. 21, pp. 379–386, 1999.

[57] S. Costa, J. Kodikara, and B. Shannon, “Salient factors controlling desiccation cracking of clay in laboratory experiments,” *Géotechnique*, vol. 63, no. 1, pp. 18–29, Jan. 2013.

List of Figures:

List of Tables:

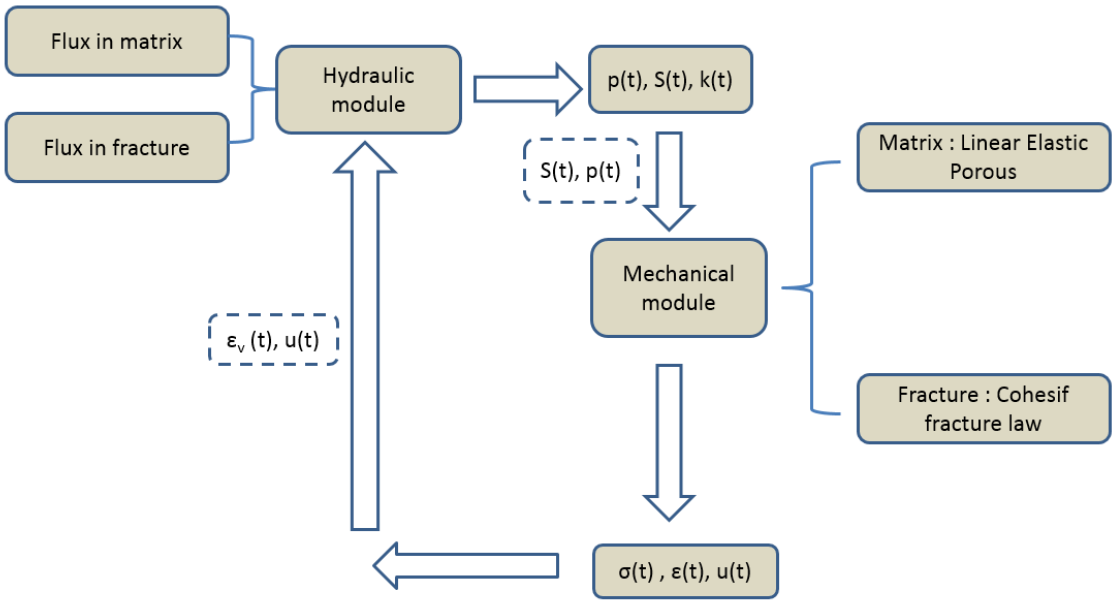

Figure 1: Scheme of the hydro-mechanical coupling

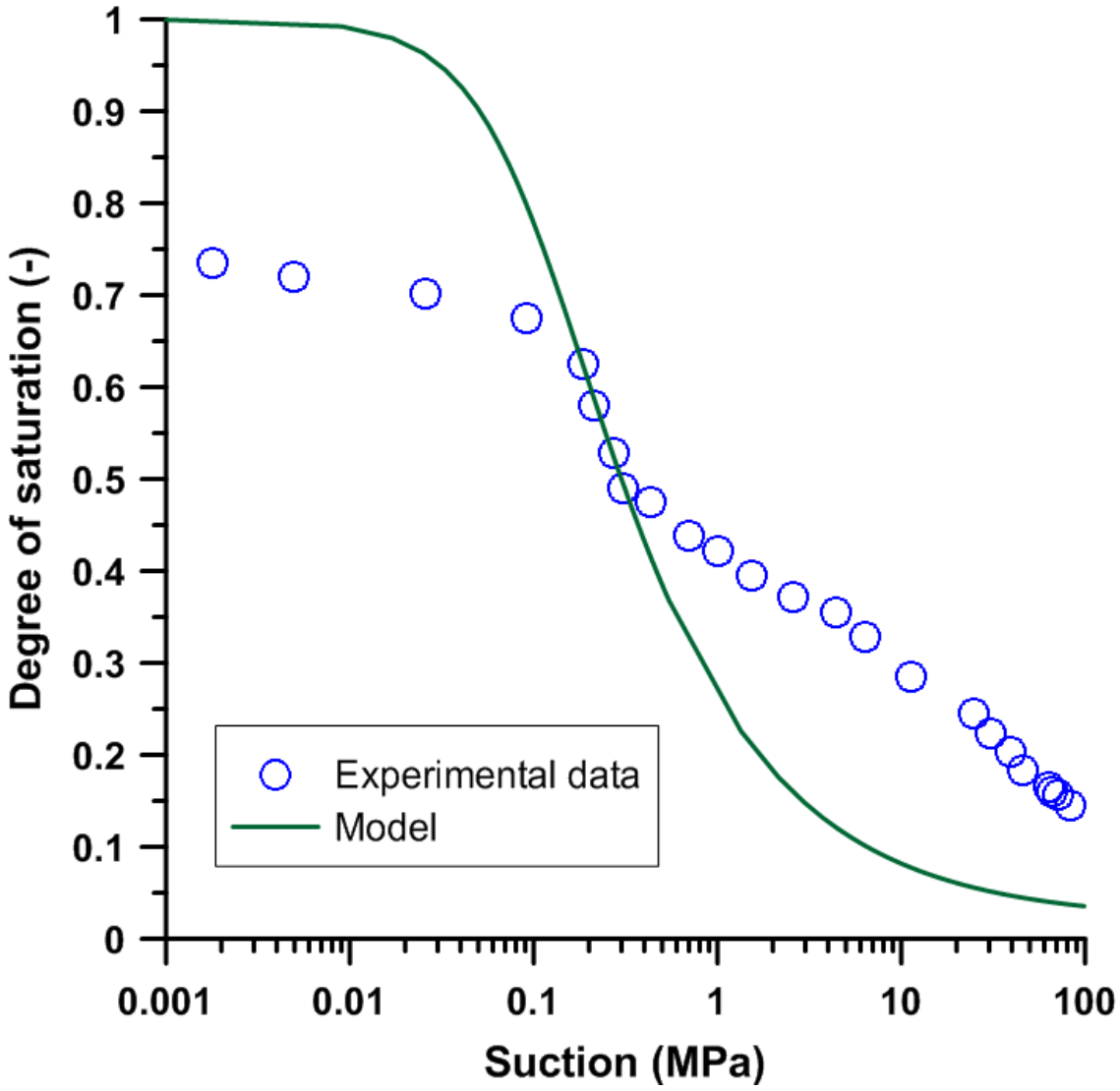

Figure 2: Water retention curve (Experimental data taken from [39])

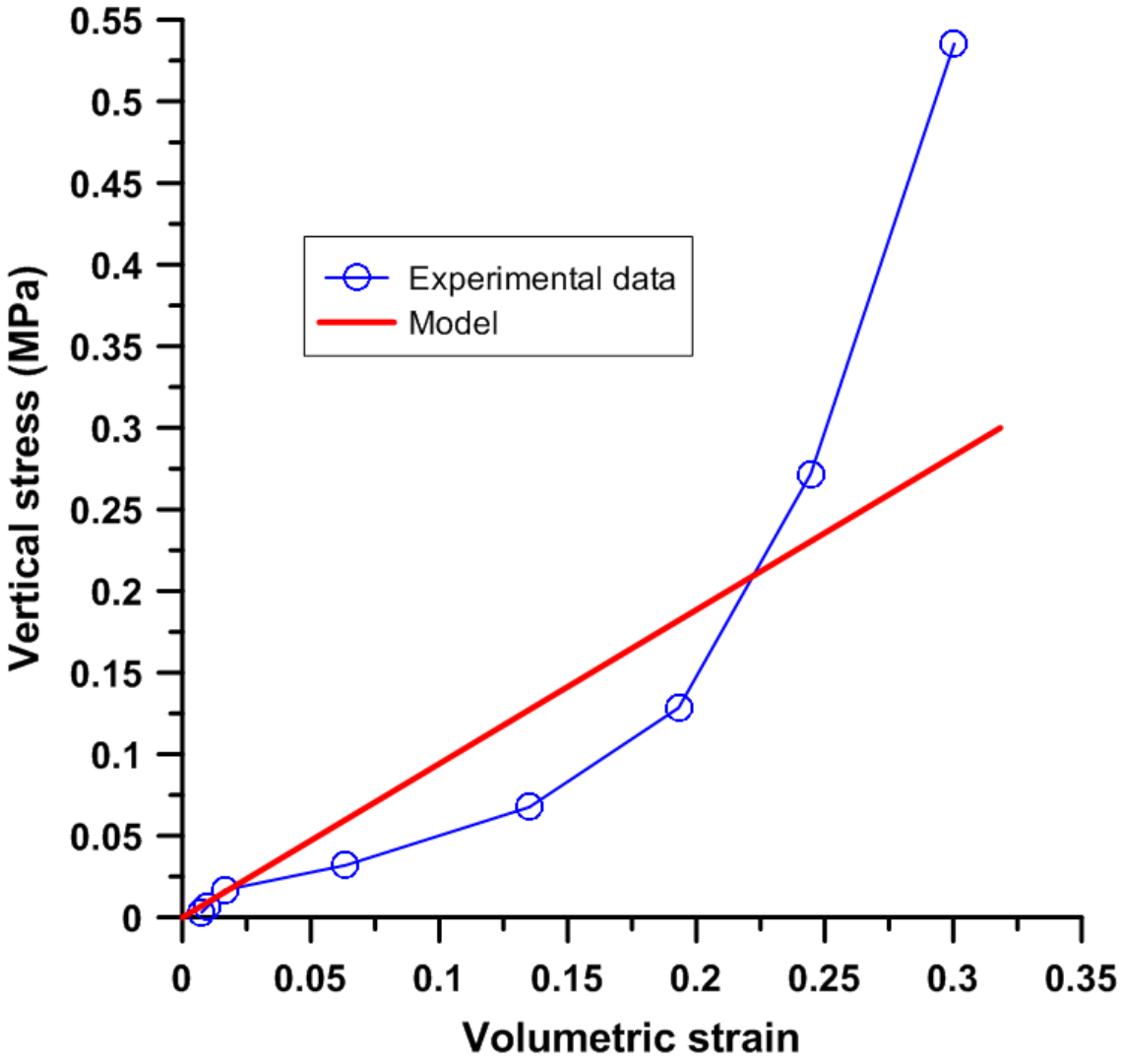

Figure 3: Compression curve obtained from oedometer test (Experimental data taken from [40])

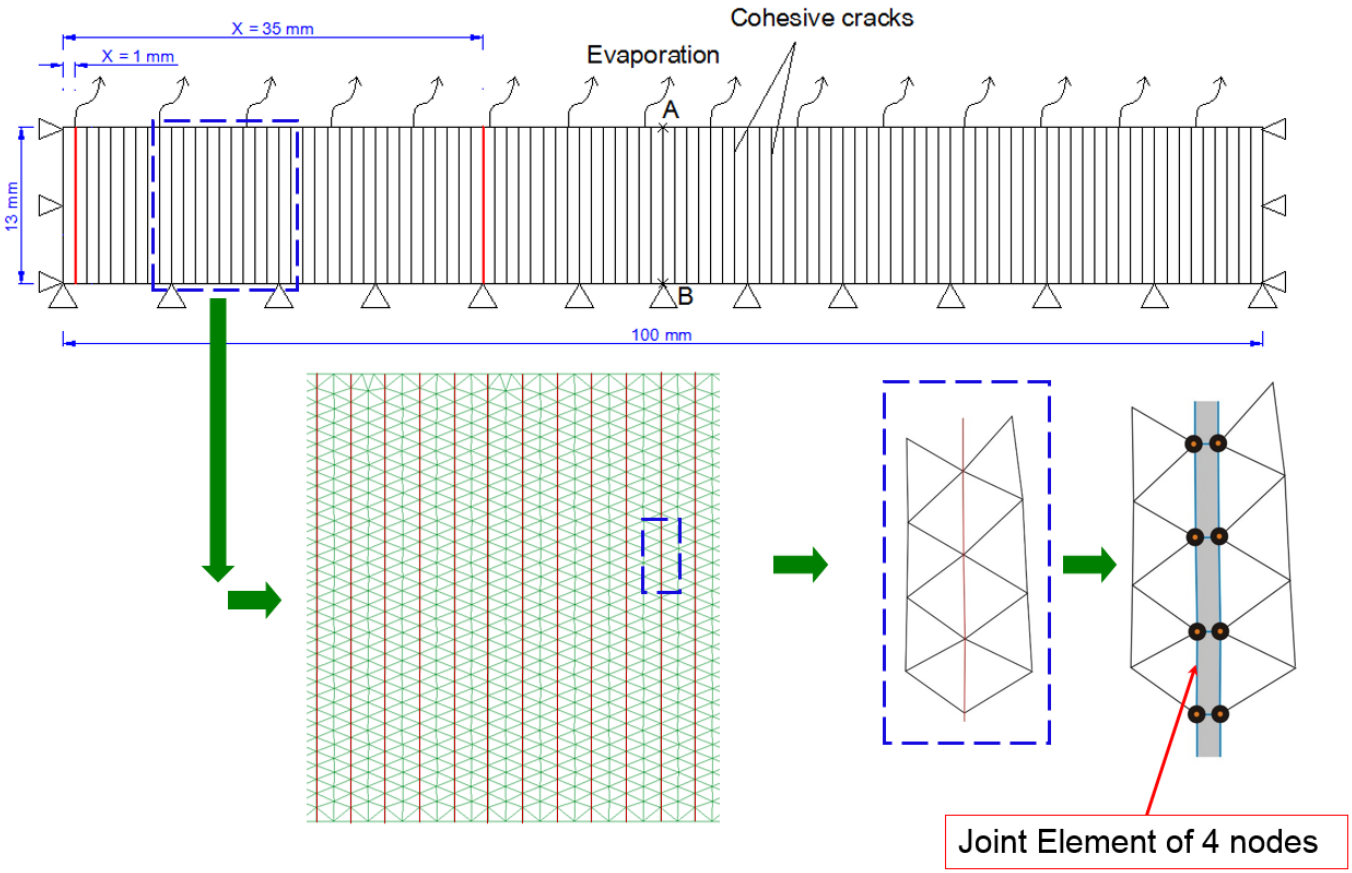

Figure 4: Geometry and boundary condition

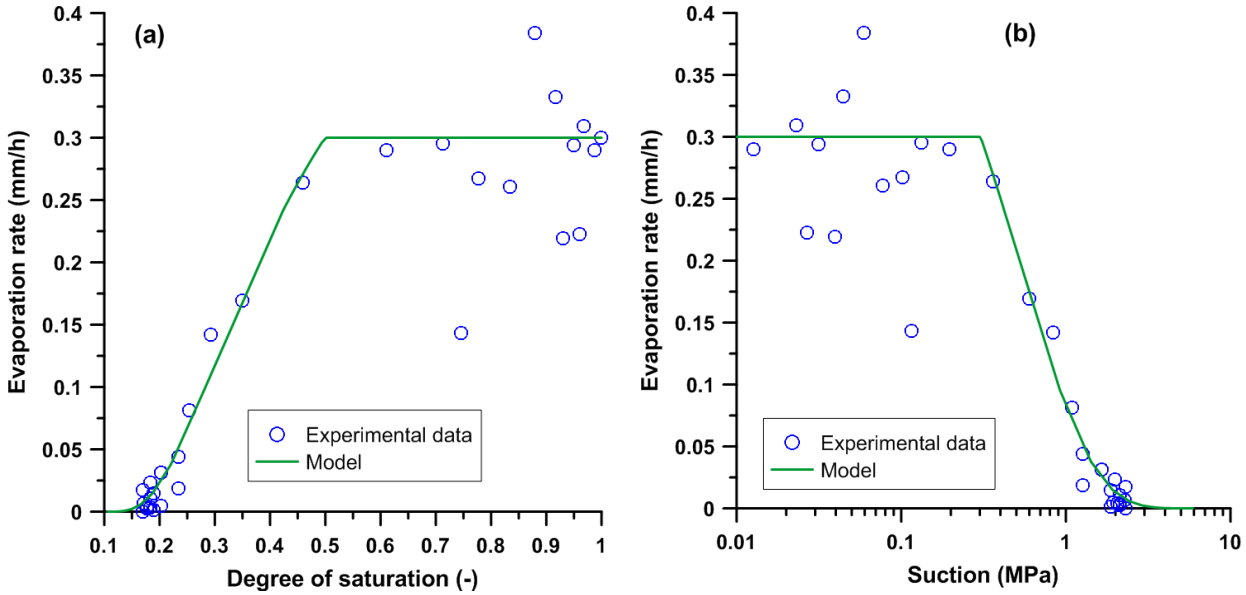

Figure 5: (a) Evaporation rate versus degree of saturation and (b) Evaporation rate versus suction (Experimental data taken from [11])

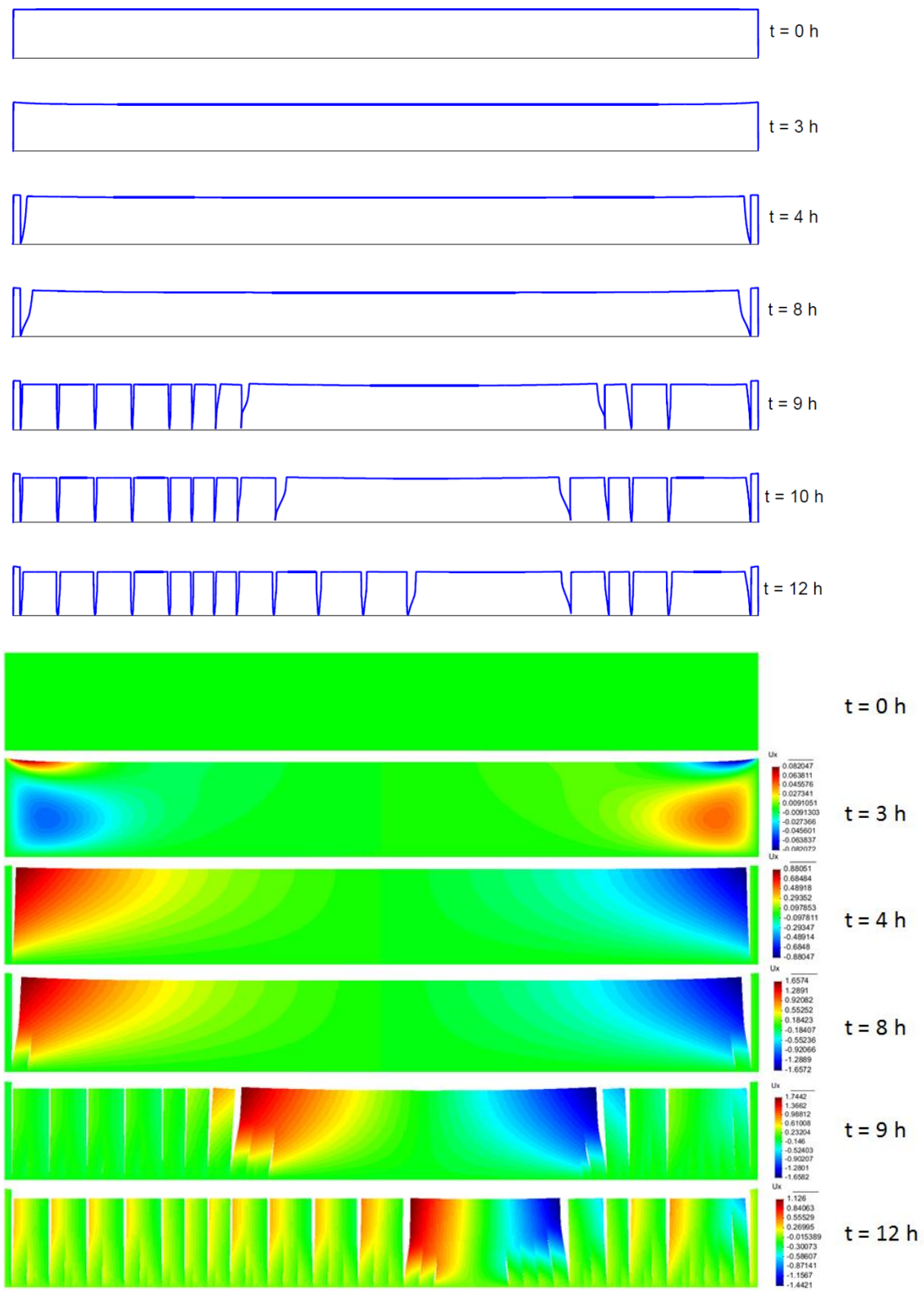

Figure 6: (a) Description of the cracks observed at various moments and (b) Distribution of horizontal displacement

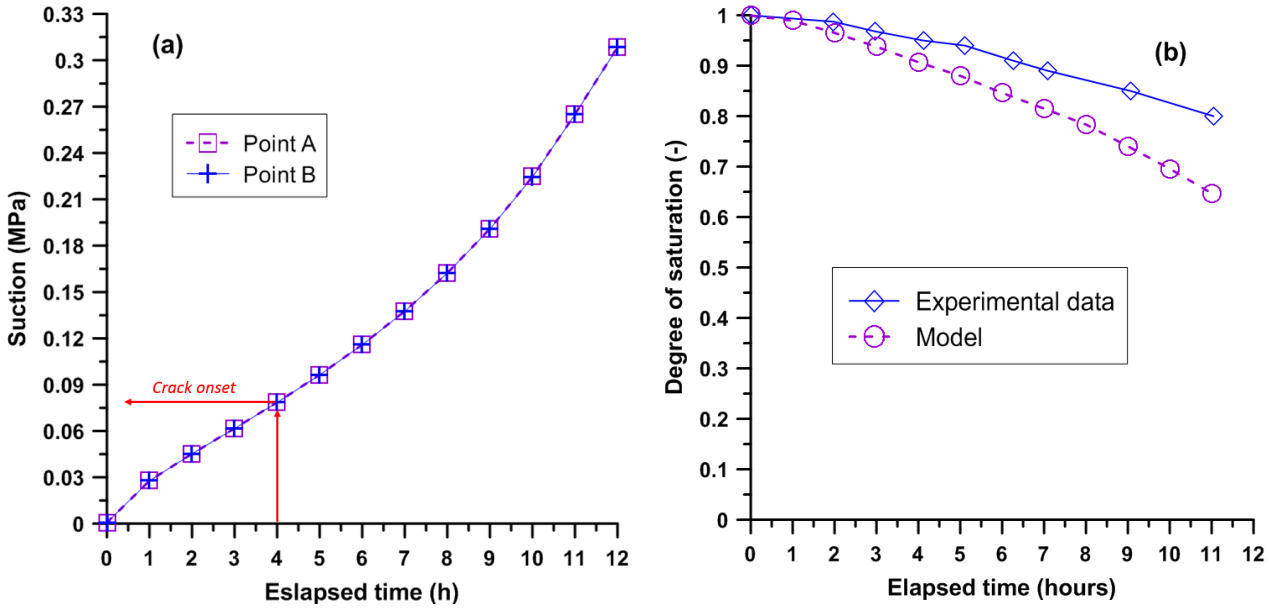

Figure 7 : (a) Suction and (b) Degree of saturation versus elapsed time. (Experimental data taken from [11])

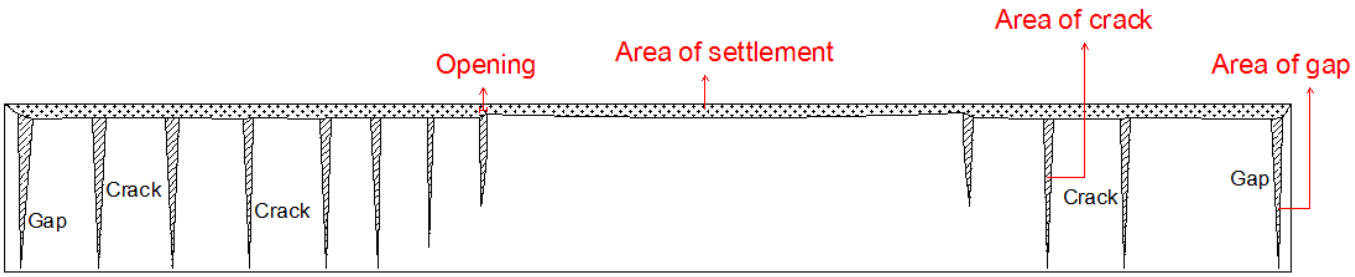

Figure 8: Scheme showing the different components of soil shrinkage

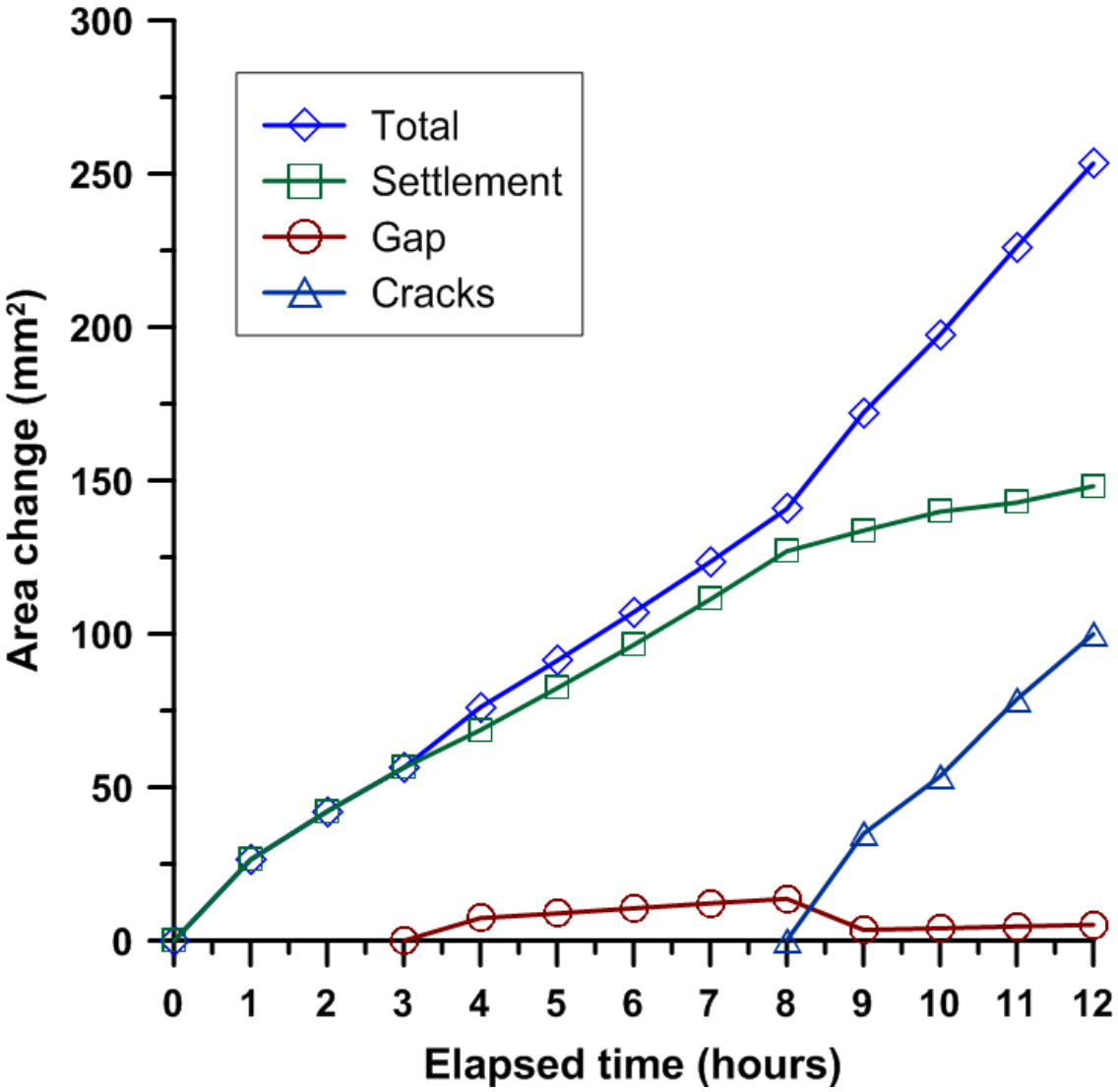

930
931
932
933 Figure 9 : Time evolution of different components of soil shrinkage
934
935
936
937

938
939
940

941

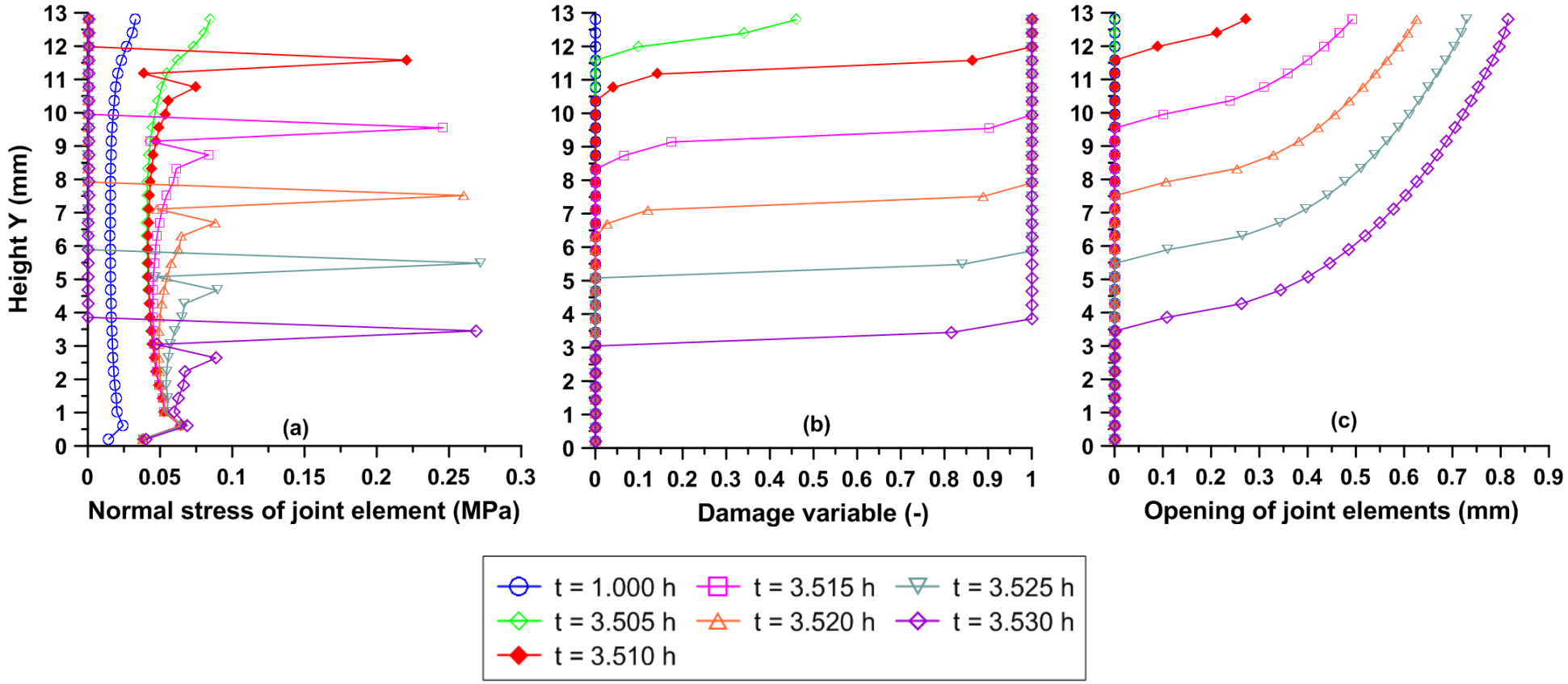

942 Figure 10: Isochrones of: (a) Normal stress, (b) Damage variable and (b) Opening of joint elements for the gap at X = 1 mm

943

944

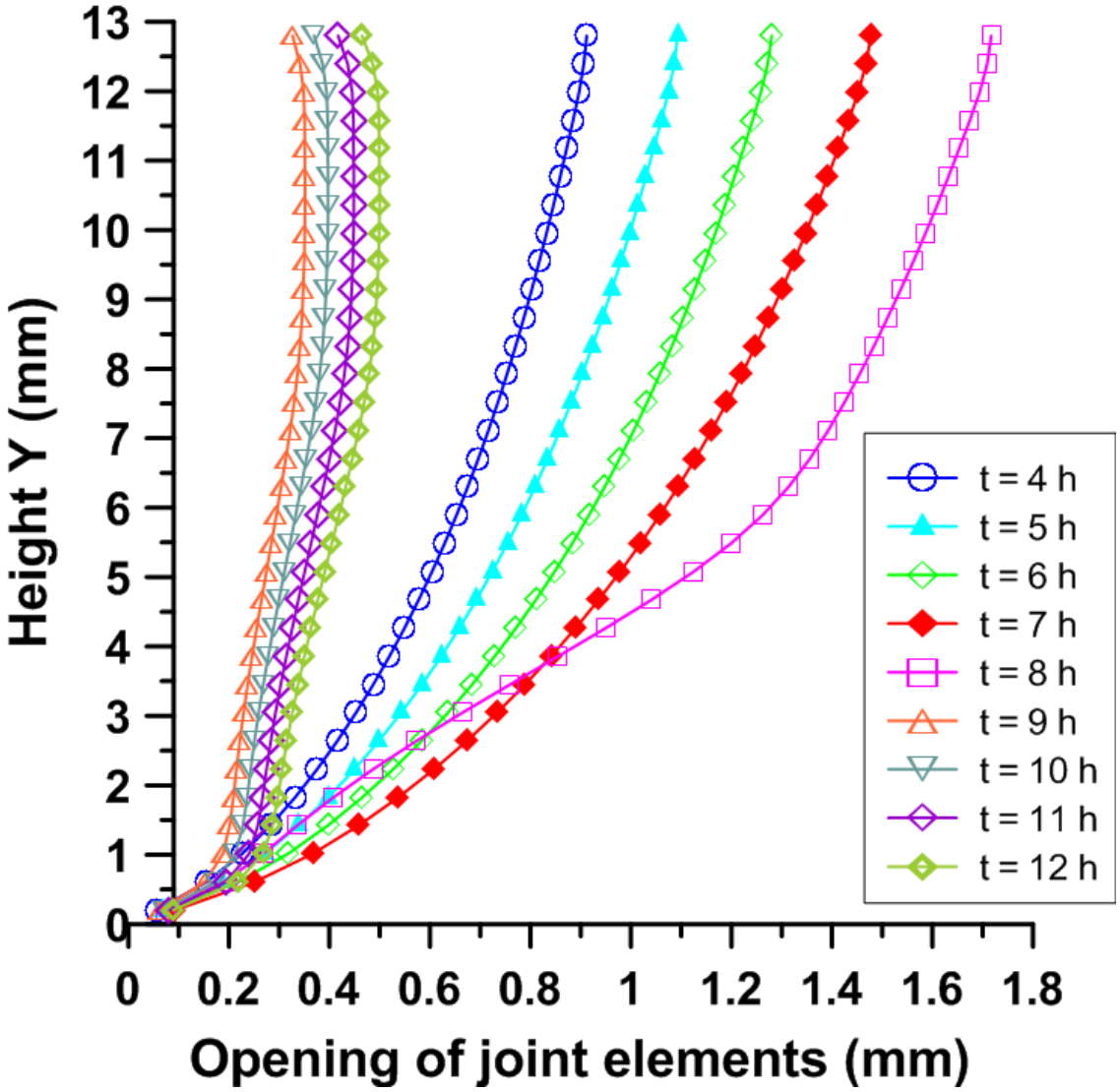

945
946
947
948

949 Figure 11: Opening of joint elements for the gap at X = 1 mm

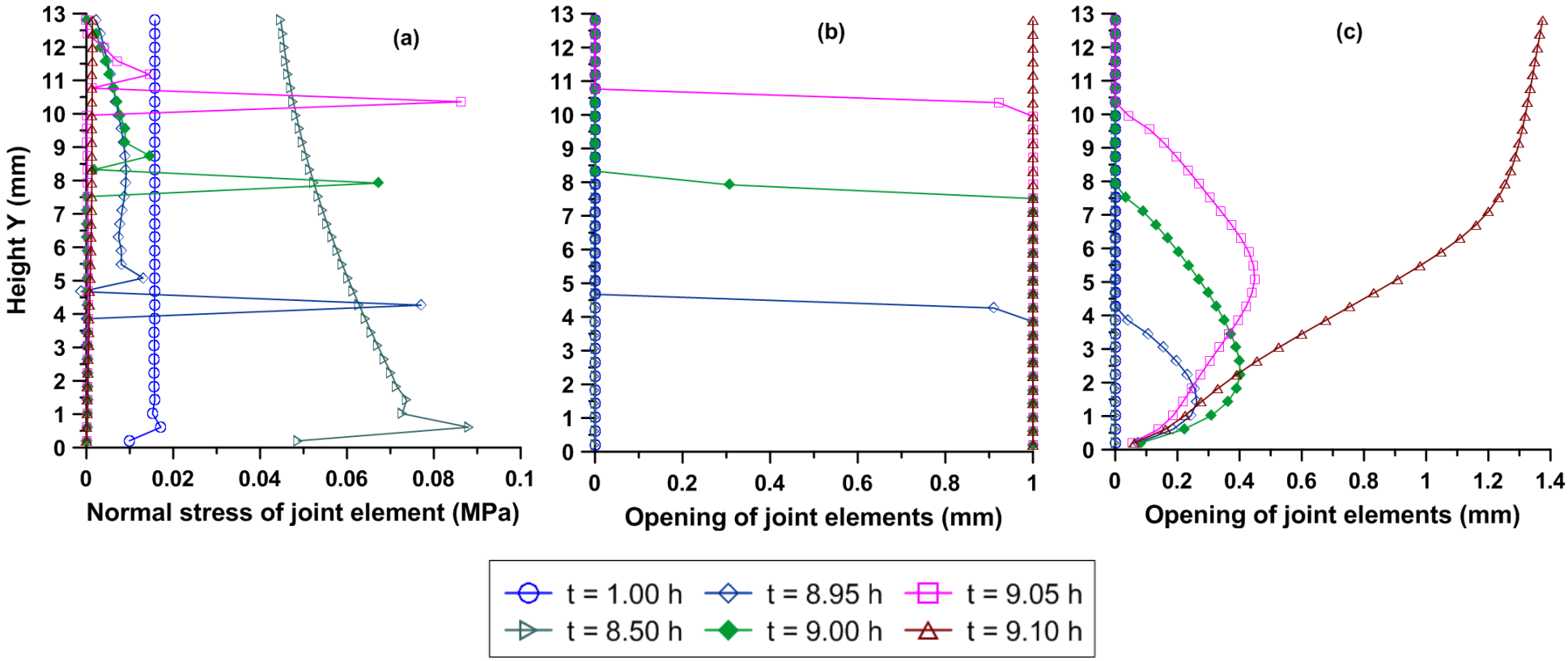

Figure 12 : Isochrones of: (a) Normal stress, (b) Damage variable and (b) Opening of joint elements for the crack at X = 35 mm

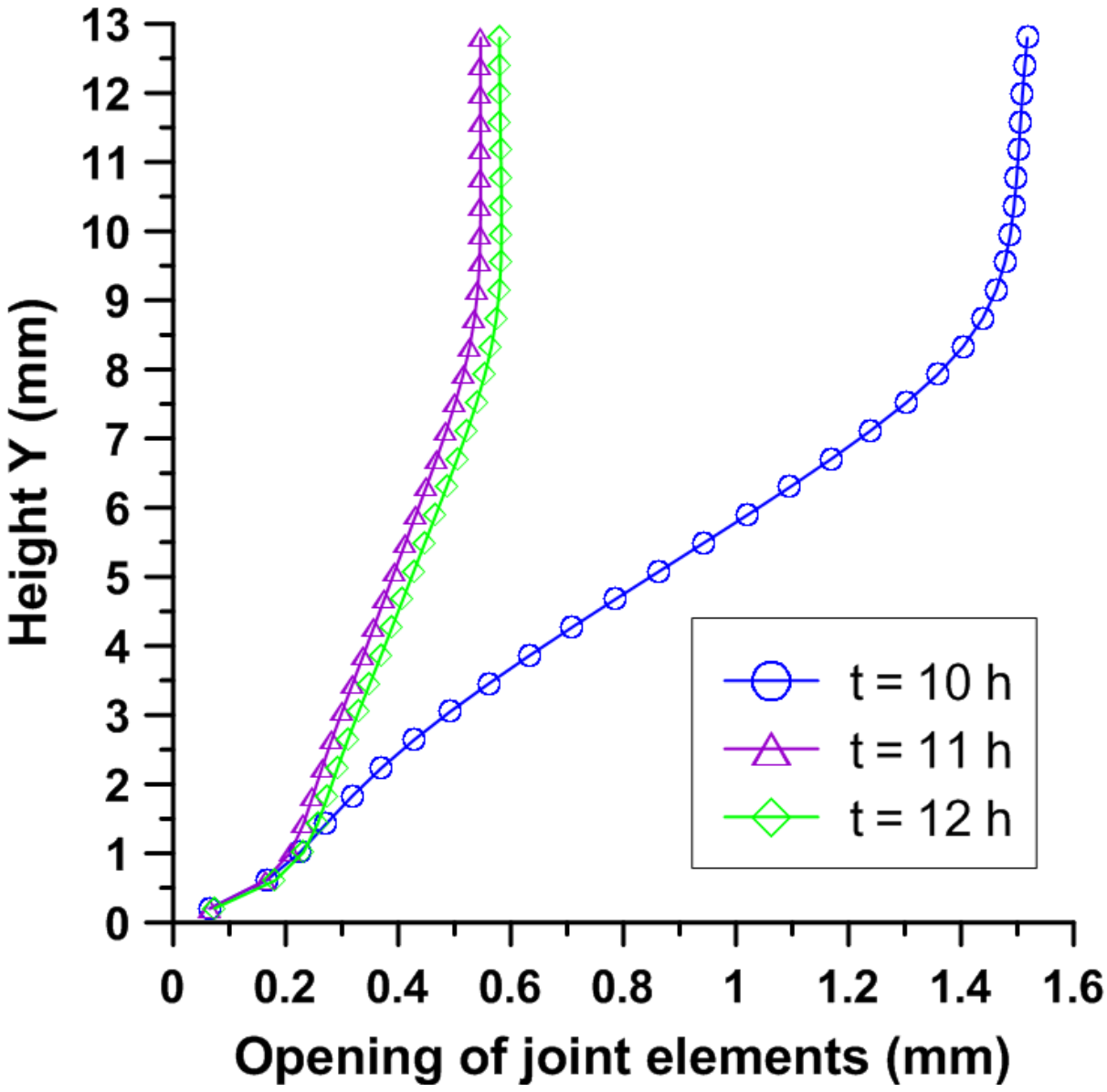

Figure 13: Opening of joint elements for the crack at X = 35 mm

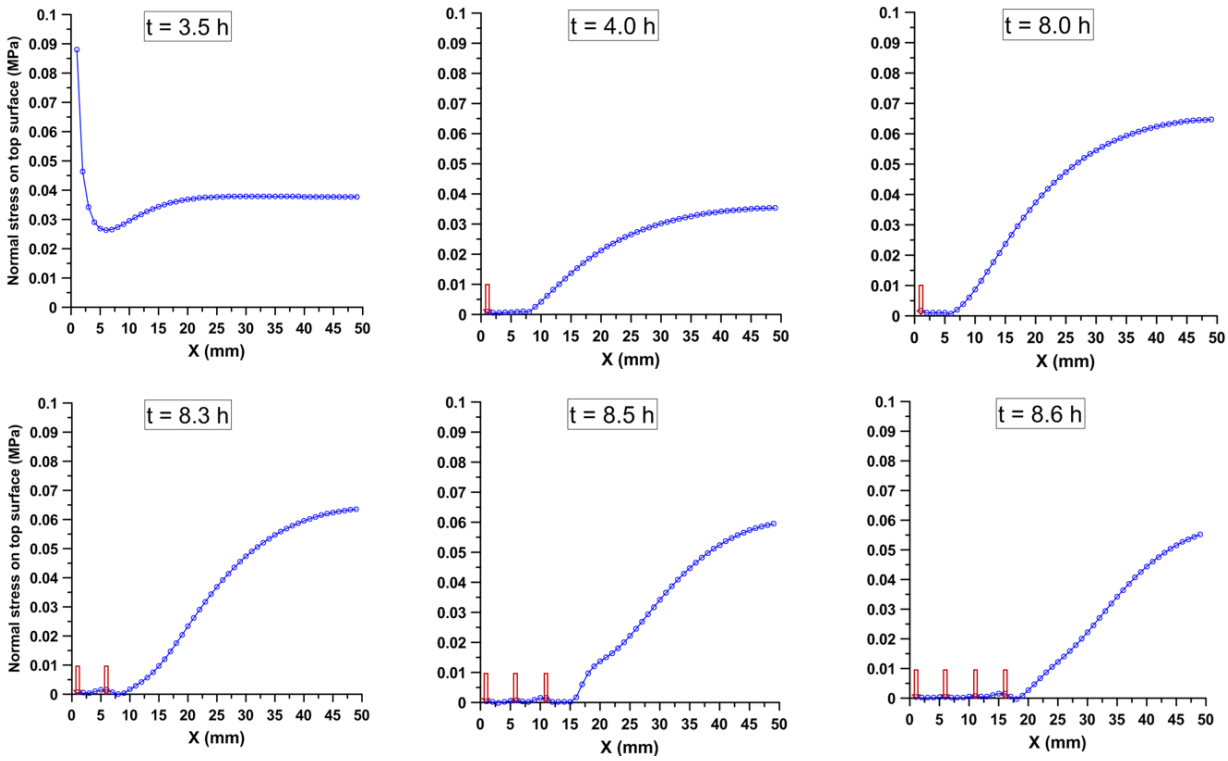

968
969
970
971 Figure 14 : Cracks position and normal stress of a half left specimen on the top surface

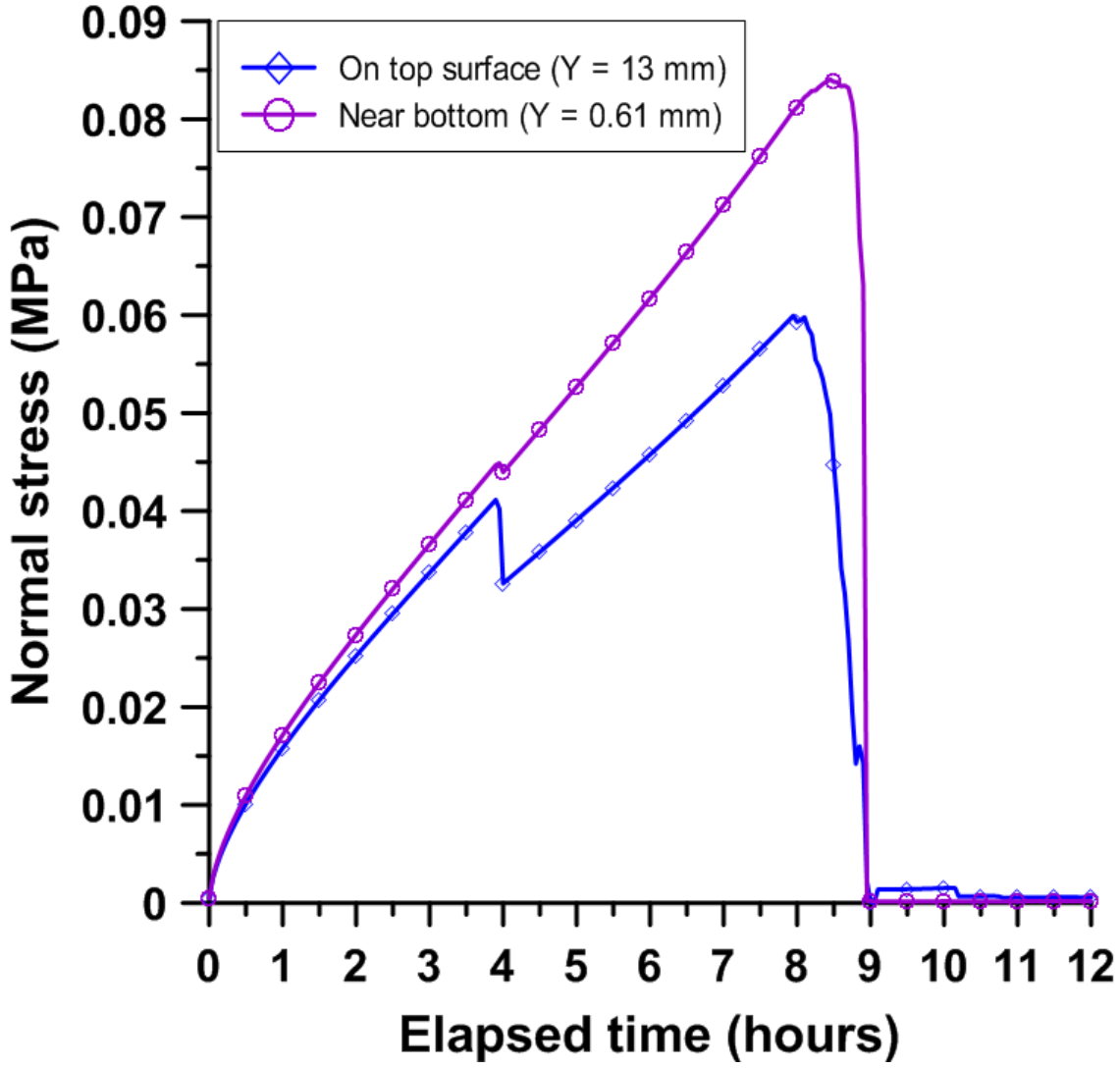

Figure 15: Evolution of normal stress of the crack at X = 35 mm

Soil	E (MPa)	ν (-)	k_s (m/s)	ϕ (-)	α (MPa^{-1})	n (-)	m (-)	S_r (-)
	1	0.3	10^{-8}	0.60	9.81	1.60	0.375	0.02

Cracks	R_{tt} (MPa/mm)	R_{nn} (MPa/mm)	$R_{tn} = R_{nt}$ (MPa/mm)	σ_R (MPa)	C_{coh} (MPa)	φ (°)	β (-)	e_0 (mm)
	1	1000	0	0.09	0.08	30	1	10^{-3}

Table 1: Parameters of soil and cohesive cracks.